Analyst

PAPER

View Article Online
View Journal



Cite this: DOI: 10.1039/d6an00320f

# Synergistic peroxidase-like activity of the Cu–Zn MOF-incorporated g-$C_3N_4$ nanozyme integrated with a smartphone-based colorimetric sensor for ciprofloxacin detection

Surendhar Sasikumar,[a] Arunjegan Amalraj[b] and Panneerselvam Perumal *[a]

Antibiotic contamination in water has emerged as a serious global threat to environmental safety and human health. Nanozyme-based optical sensors have demonstrated significant potential for the rapid and highly sensitive detection of antibiotics in environmental samples. Therefore, herein, we have developed a new synergistic hybrid nanozyme (Cu–Zn-MOF/g-$C_3N_4$) based on Cu–Zn-MOF-incorporated g-$C_3N_4$ nanosheets. This hybrid nanozyme enables the oxidation of TMB through OH radical generation *via* a Fenton-like reaction involving $Cu^{2+}/Cu^{+}$ on the nanozyme surface, while the framework stability is achieved through stabilization by $Zn^{2+}$, and the conjugated g-$C_3N_4$ enhances electron transfer for the generation of reactive oxygen species. Importantly, the peroxidase-like activity of Cu–Zn-MOF/g-$C_3N_4$ was selectively and significantly enhanced in the presence of ciprofloxacin (CIP) owing to a specific interaction between the nanozyme and CIP. This interaction further accelerates electron transfer, thereby promoting efficient oxidation of TMB. Furthermore, the proposed colorimetric CIP sensor exhibits a rapid response toward CIP and a broad linear range of 2–200 μM with a low detection limit of 0.66 μM. To meet the requirements for on-site colorimetric detection, the system was integrated with a portable smartphone-assisted RGB platform, enabling the *in situ* determination of CIP in environmental water samples. These findings highlight the critical role of bimetallic coordination in modulating the electronic properties of hybrid nanomaterials, thereby establishing this system as a promising platform for rapid, cost-effective, and sensitive visual detection in environmental monitoring applications.

Received 24th March 2026,
Accepted 12th May 2026

DOI: 10.1039/d6an00320f

rsc.li/analyst



## 1 Introduction

At sub-therapeutic concentrations, antibiotics can adversely affect non-target organisms such as algae, invertebrates, and other aquatic species, influencing their growth, reproduction, and overall community structure. A major concern is that continuous exposure to these low levels promotes the development of antibiotic-resistant bacteria and resistance genes. These resistance traits can spread through water, soil, and food chains, eventually reaching humans and animals.[1–5] Ciprofloxacin (CIP) is a broad-spectrum antibiotic belonging to the fluoroquinolone class that is frequently used to treat a variety of bacterial infections, such as respiratory, gastrointestinal, urinary tract, and certain skin and bone infections. It is effective against many resistant infections because it inhibits the growth and multiplication of bacteria.[6] Nevertheless, despite its benefits, CIP has numerous drawbacks. In rare instances, it may result in more serious side effects like tendon rupture, nerve damage, or irregular heartbeat. Other side effects include nausea, diarrhoea, headaches, and dizziness.[7–9] Laxminarayan and Chaudhury *et al.* investigated fluoroquinolone resistance in *Escherichia coli* (*E. coli*), where the resistance increased from 78% in 2008 to 85% in 2013. In comparison, fluoroquinolone resistance in *Salmonella typhi* isolates increased from 8% in 2008 to 28% in 2014. Dreyer *et al.* found that, out of 331 multidrug-resistant isolates of the *Mycobacterium tuberculosis* complex, 36% of the isolates were resistant to fluoroquinolones, contributing to the increase of pre-extensively drug-resistant isolates in Mumbai, India.[10,11] Maximum residue levels (MRLs) have also been established by several organizations and countries to regulate the illegal use of antibiotics in many food products. The European Union has also established maximum residue limits (MRLs) for certain fluoroquinolones including CIP in certain edible animal tissues (30 g $kg^{-1}$ in various edible animal tissues). In India, the maximum residue limit of MOX in food samples has been

[a]Department of Chemistry, SRM Institute of Science and Technology, Kattankulathur, 603203 Tamil Nadu, India. E-mail: panneerp1@srmist.edu.in, panneerchem82@gmail.com
[b]School of the Environment and Safety Engineering, Jiangsu University, Zhenjiang 212013, China

fixed at 1.0 g $kg^{-1}$.[12,13] Different sensing methods have been reported for CIP sensing, including high-performance liquid chromatography (HPLC), liquid chromatography-mass spectrometry (LC-MS), electrochemical sensing, and fluorescence sensing.[14–20] Although these techniques can achieve outstanding sensitivity and accuracy, the requirements for sophisticated instrumentation, complicated sample preparation, pretreatment, and operational procedures hinder their practical application. Colorimetric sensing has emerged as a promising alternative due to its low cost, simple procedure, rapid response, and highly sensitive detection capability. However, the catalytic properties of nanozymes are crucial factors influencing system performance, and highly efficient sensors are still desirable.

Metal–organic frameworks (MOFs), comprising both inorganic and organic components, have been employed in optical sensors for decades. MOFs, made up of inorganic cationic nodes and organic ligands, are a novel class of porous materials. Simple metal ions or clusters with organic linkers form highly porous crystalline structures with various functional groups. Many MOF-based detection methods, like electrochemical, fluorescence, colorimetric and surface-enhanced Raman scattering methods, have shown good sensitivity and selectivity for the detection of many hazardous chemicals in agricultural and environmental applications.[21–25] Recently, bimetallic MOFs have received extensive research attention for colorimetric sensing because of their improved catalytic performance compared to monometallic MOFs. In these systems, two different metal ions are co-linked within the same framework to generate synergistic interactions similar to those of natural enzymes (*e.g.*, peroxidase or oxidase). The cooperative metal centres (*e.g.*, Fe/Cu, Ni/Co, or Mn/Fe) increase the abundance of active catalytic sites and promote the rapid transfer of electrons, highly accelerating $^{\bullet}OH$ decomposition and generating more reactive $^{\bullet}OH$ radicals. Consequently, chromogenic reactions (*e.g.*, TMB oxidation) can be strongly enhanced, producing a distinctive change in color for affordable optical sensing. Therefore, it is believed that these bimetallic MOFs are more sensitive, selective and more catalytically stable than monometallic MOFs for the optical detection of hazardous contaminants in the environment.[26–28] Nevertheless, some aqueous metal–organic framework systems have been extensively investigated. For example, the Cu–Zn framework system has the potential to show peroxidase-mimicking activity since $Cu^{2+}$ ions can actively be involved in redox reactions, while $Zn^{2+}$ can efficiently modulate the electronic and structural environment. However, one of the limitations of MOFs in sensing applications is their poor electrical conductivity and charge-transfer capability.[29,30]

Two-dimensional (2D) materials, a class of crystalline solids, consist of mono- or bi-layer structures. Since the groundbreaking isolation of graphene in 2004, the 2D family has drawn enormous research interest and enthusiasm due to their extraordinary physical, chemical and electronic properties, which are radically different from those of their bulk forms.[31] The strong quantum confinement effect, high surface-to-volume ratio, and flexible band structure, which can be widely modulated, benefit a broad spectrum of potential applications. In addition to graphene, transition metal dichalcogenides, hexagonal boron nitride, MXenes and black phosphorus have been recognized as part of the 2D family. Among these, graphitic carbon nitride (g-$C_3N_4$) has been identified as a promising metal-free 2D material due to its high chemical stability, visible-light response and low synthesis cost.[32] g-$C_3N_4$ has a moderately broad band gap of *ca.* 2.7 eV, a graphite-like layered structure, and has been extensively studied for various applications in photocatalysis, electrocatalysis, environmental remediation and sensing. The nitrogen-rich constitution of g-$C_3N_4$ offers numerous active sites and interfacial interactions with metal-based materials while also acting as an electron mediator for enhancing charge separation and transfer. However, pristine g-$C_3N_4$ still has deficiencies like low electrical conductivity, a fast charge recombination rate and an agglomeration tendency, which are unfavourable for catalytic activity. One of the approaches to overcome these disadvantages is coupling g-$C_3N_4$ with other functional materials (especially MOFs), which could obviously enhance the catalytic performance by promoting electron transport, facilitating electroactive sites and enhancing interfacial coupling. Hence, the combination of MOFs and g-$C_3N_4$ might be an ideal method to construct an efficient catalytic sensing system.[33–35]

Transition metals are characterised by variable oxidation states and a strong propensity to form complex compounds. Their partially filled d orbitals give them a wide range of unique physical and chemical properties. These elements typically display various oxidation states, robust metal-binding ability with a range of ligands, and the generation of complex ions, in addition to distinguished characteristics such as optimized electrical conductivity and thermal conductivity, mechanical strength, and remarkable catalytic activity. Transition metals are critical in many scientific and industrial fields. They are important in metallurgy, chemical catalysis, energy conversion and storage, environmental cleanup, electronics, and nanotechnology. Their adjustable electronic structures and adaptable chemical properties have prompted a lot of research, leading to progress in green chemistry, sustainable energy, and next-generation functional materials.[36–43] Preeti Sharma *et al.* have developed Cu-MOF@TMB-integrated test strips to identify the critical biomarkers for metabolic and renal disorders, with a limit of detection of 0.941 ppm.[44] Komal *et al.* have developed a novel N-CND/PAni-modified molecularly imprinted polymer for the detection of CIP using fluorescence and colorimetric sensors. The limits of detection are 70 pM for the fluorescent signalling platform and 3.5 nM for the colorimetric probe, with a linear range of 0.038–200 nM.[45]

In this work, a bimetallic Cu–Zn-MOF/g-$C_3N_4$ composite was synthesized through a solvothermal method. As is shown, the composite exhibits peroxidase-like activity, which was used to establish a colorimetric sensing platform for the rapid and precise detection of CIP. The synergistic interaction between

 

the $Cu^{2+}/Cu^{+}$ and $Zn^{2+}/Zn^{+}$ redox pairs significantly enhanced electron transfer, thereby boosting the catalytic oxidation capability of the system. Strong coordination occurred between CIP and $Cu^{2+}$ in Cu–Zn-MOF/g-$C_3N_4$, which triggered a Fenton-like reaction and promoted the generation of $^{\bullet}OH$ radicals. The produced $^{\bullet}OH$ efficiently catalysed the oxidation of the chromogenic substrate 3,3′,5,5′-tetramethylbenzidine (TMB), converting colourless TMB into blue oxidized TMB (oxTMB). Notably, the resulting color transitions are discernible to the naked eye for qualitative assessment; for precise on-site quantification, this system was coupled with a smartphone-assisted RGB colorimetric platform. This portable approach enables real-time determination of CIP in environmental matrices, including drinking, tap, and lake water, yielding high recovery rates and excellent selectivity.

# 2 Experimental

## 2.1 Materials

Copper nitrate trihydrate ($Cu(NO_3)_2{\cdot}3H_2O$), zinc nitrate hexahydrate ($Zn(NO_3)_2{\cdot}6H_2O$), 2-aminoterephthalic acid (BDC-$NH_2$), *N*,*N*-dimethylformamide (DMF) (99.98%), hydrogen peroxide ($H_2O_2$), 3,3′,5,5′-tetramethylbenzidine (TMB), and other chemicals were acquired from SRL Pvt Ltd. Each of the substances listed above was of the highest purity and analytical grade.

## 2.2 Synthesis of g-$C_3N_4$

Melamine was used as a precursor, and following a described process, g-$C_3N_4$ was prepared by thermal polymerisation.[46] The melamine was transferred into a covered alumina crucible and heated to 550 °C in a muffle furnace with a heating ramp of 25 °C $min^{-1}$ under a static air atmosphere. The crucible was held at this temperature for 4 h and allowed to cool naturally to room temperature. The yellow solid obtained was then ground to a fine powder to obtain bulk g-$C_3N_4$. The product was then dispersed in 30 mL of deionized water and ultrasonicated for 1 h. During ultrasonication, the particle size decreased significantly, and the bulk was exfoliated to form a stable aqueous suspension.

## 2.3 Synthesis of Cu–Zn-MOF

Initially, $Cu(NO_3)_2{\cdot}3H_2O$ (1 mM) and $Zn(NO_3)_2{\cdot}6H_2O$ (1 mM) were dissolved in 30 mL of DMF to prepare precursor solution I. Meanwhile, precursor solution II was prepared by dissolving BDC-$NH_2$ (2 mM) in DMF (30 mL). Subsequently, 0.5 mL of solution II was added dropwise to solution I under continuous magnetic stirring to obtain a homogeneous mixture. After that, the solution turned dark green upon stepwise addition of solution II under continuous stirring. The resulting solution was transferred into a 100 mL Teflon-lined stainless-steel autoclave and heated to 120 °C for 24 h. The powder was isolated by centrifugation after cooling to room temperature and washed repeatedly with DMF and ethanol to remove impurities. Then, the powder was dried overnight at 60 °C in a drying oven to obtain bright green Cu–Zn-MOF powder.

## 2.4 Synthesis of Cu–Zn-MOF/g-$C_3N_4$

Cu–Zn-MOF/g-$C_3N_4$ was prepared at a 0.7 : 1 ratio of g-$C_3N_4$ : Cu–Zn-MOF. Bulk g-$C_3N_4$ was dispersed in 30 mL of ethanol and ultrasonicated for 30 min to obtain solution A. Then, 0.5 mL of the prepared Cu–Zn-MOF solution, denoted as solution B, was added dropwise to solution A. The suspension was poured into a 100 mL stainless-steel autoclave lined with a Teflon capsule. The autoclave was heated to 120 °C for 24 h. After the reaction, the autoclave was cooled to room temperature. The precipitate was collected by centrifugation and washed several times with solvents such as DMF and ethanol. The powder was then dried in an oven at 60 °C overnight. Finally, the greyish-green Cu–Zn-MOF/g-$C_3N_4$ composite powder was obtained (Scheme 1).

## 2.5 Peroxidase-like activity of the Cu–Zn-MOF/g-$C_3N_4$ nanozyme

The peroxidase-like activity of the Cu–Zn-MOF/g-$C_3N_4$ nanozyme was investigated using a typical TMB and $H_2O_2$ colorimetric system. In a standard reaction, 200 μL of 10 mM $H_2O_2$, 900 μL of 40 μM TMB, and 500 μL of acetate buffer (pH 4.0) were mixed, followed by the addition of 200 μL of the Cu–Zn-MOF/g-$C_3N_4$ nanozyme dispersion. Upon incubation at room temperature, a distinct blue color rapidly developed, accompanied by a strong absorbance peak at 652 nm, confirming the oxidation of TMB. In contrast, control experiments without the nanozyme showed negligible color change. The higher catalytic activity of Cu–Zn-MOF/g-$C_3N_4$ than that of pristine g-$C_3N_4$ and single-metal systems evidences the synergistic effect of Cu and Zn species. The peroxidase-like activity can be ascribed to the redox couple of $Cu^{2+}/Cu^{+}$ in conjunction with the modification of the electronic structure induced by Zn species, which promotes the activation of $H_2O_2$ and accelerates electron transfer on g-$C_3N_4$.

## 2.6 Real sample analysis

The applicability of the Cu–Zn-MOF/g-$C_3N_4$ sensor for real environmental analysis was evaluated using drinking water, tap water, and lake water samples. The drinking water and tap water samples were collected from the laboratory, and SRM Lake water samples were purchased. All the samples were centrifuged for 10 min, and insoluble impurities were eliminated by filtration using a 0.22 M membrane filter. After that, the water samples were mixed with the Cu–Zn-MOF/g-$C_3N_4$ analyte, and the reaction time was 2 min. The color change was monitored using UV-vis absorption spectroscopy.

# 3 Results and discussion

## 3.1 Structural and morphological analysis

The analysis of p-XRD was carried out to identify the crystalline phase, structural formation and composition. Fig. 1a reveals the g-$C_3N_4$ pattern, and the diffraction peaks formed at $2\theta$ = 12.7° (1 0 0) correspond to the interplanar structural packing of heptazine, while the peak at $2\theta$ = 27.2° (0 0 2) relates to the characteristic interlayer stacking structure.[47] The

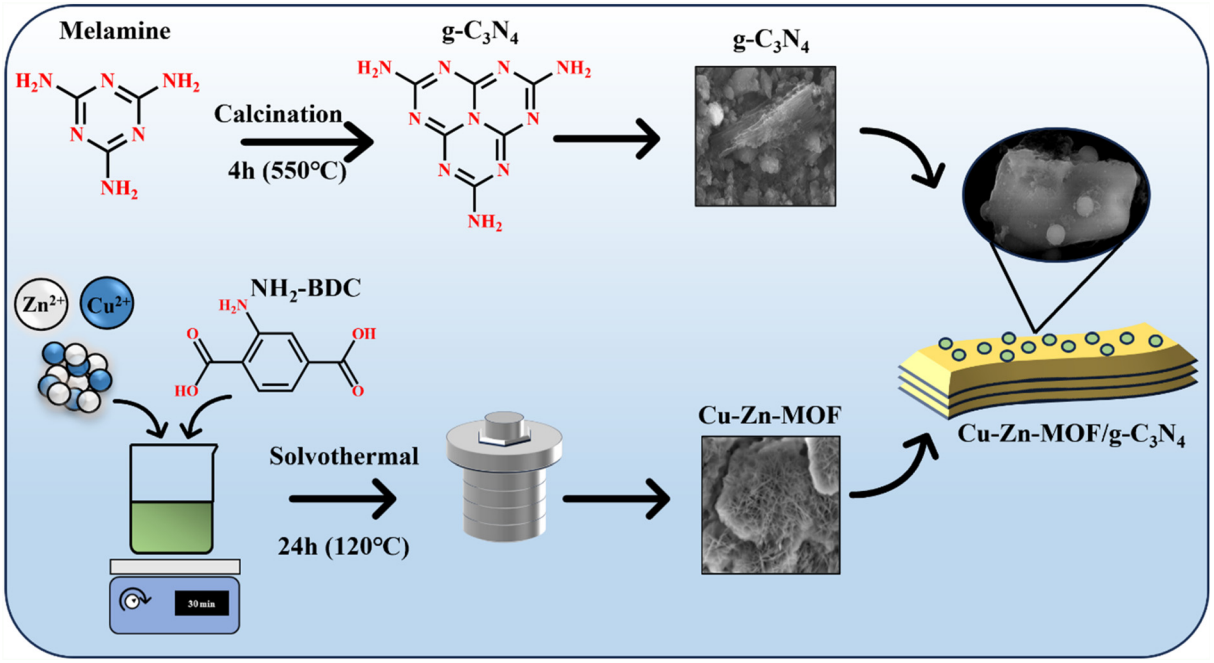


**Scheme 1** Schematic representation of the stepwise synthesis of Cu–Zn-MOF/g-$C_3N_4$.

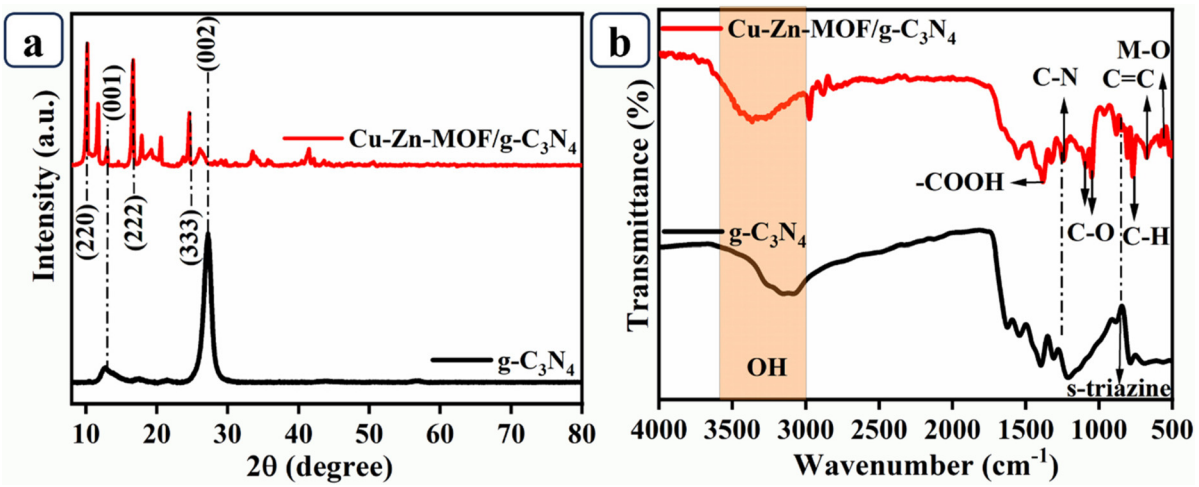


**Fig. 1** (a) p-XRD patterns and (b) FTIR spectra of g-$C_3N_4$ and Cu–Zn-MOF/g-$C_3N_4$.

characteristic peaks of Cu–Zn-MOF/g-$C_3N_4$ at 10.2°, 16.5°, and 24.5° correspond to the planes of (2 2 0), (2 2 2), and (3 3 3), with the main peak at 10.2° representing an intermediate reflection between the two parent MOFs (9.1° and 10.4°). The peak shift provides definitive evidence for the co-integration of $Cu^{2+}$ and $Zn^{2+}$ to form a single, crystalline bimetallic framework. Furthermore, the peaks present at 13.2° (0 0 1) and 27.3° (0 0 2) confirm the successful incorporation of the g-$C_3N_4$ support.[48] Fig. S1a displays the p-XRD patterns of Cu-MOF, with characteristic peaks observed at $2\theta$ = 9°, 13.5°, 16.3°, and 24.5°, corresponding to the (1 1 0), (0 2 0), (3 3 3), and (2 2 2) planes, respectively. In addition, Zn-MOF shows a characteristic diffraction peak at $2\theta$ = 10.4°, which corresponds to the (2 2 0) lattice plane.[49–51]

FTIR spectroscopy was used to identify the functional groups and confirm the chemical bonding in the synthesized materials. The FTIR spectra of the Cu–Zn-MOF/g-$C_3N_4$ composite are presented in Fig. 1b. The Cu–Zn-MOF/g-$C_3N_4$ composite displays a broad vibrational band spanning in the range of 3400–3200 $cm^{-1}$, which is attributed to the O–H and N–H functional groups. The broadness and magnitude of this band at 3380 $cm^{-1}$ suggest significant intermolecular H-bonding between the amino groups of g-$C_3N_4$ and the oxygen-based linkers of the MOF. The broad band at 3400 $cm^{-1}$ can be

attributed to the O–H stretching vibration, which could be due to adsorbed water. Such broad features are attributed to hydrogen-bonded O–H in porous materials.[52,53] The stretching frequency at 1551 $cm^{-1}$, corresponding to the C=C functional group, exhibits a blue shift, suggesting an increase in the bond force constant, potentially resulting from the electronic synergy between the dual metal centres (Cu/Zn). A similar blue shift at 138 $cm^{-1}$ is assigned to the symmetric stretching mode of the coordinated carboxylate (–COOH) group,[54] suggesting that the bimetallic environment alters the uniform electron distribution within the metal–ligand coordination sphere. The band at 1245 $cm^{-1}$, which corresponds to the C–N stretching vibration, suggests possible contact bonding at the heterojunction between the nanoparticles and the g-$C_3N_4$ sheets. This peak, along with changes in the benzene ring vibration at 768 $cm^{-1}$, confirms π–π stacking interactions and possible electronic coupling between the MOF aromatic rings and the g-$C_3N_4$ layers. The bands at 1091 and 1052 $cm^{-1}$ belong to the C–O group. There is a red shift at 675 $cm^{-1}$ representing the C=C bend vibration. Furthermore, the bands at 583 and 555 $cm^{-1}$, which correspond to the vibrational frequencies of M–O, also show a marked red shift. This shift to lower wavenumbers implies a slight weakening of the metal–oxygen bonds, potentially due to electron back-donation from the nitrogen-rich g-$C_3N_4$ sheets to the Cu/Zn d-orbitals. The stretching vibrations of O–H in g-$C_3N_4$ are within 3000–3600 $cm^{-1}$, while aromatic C–N of the heterocyclic peaks are observed at 1211, 1310, 1396, 1546 and 1624 $cm^{-1}$. In addition, the peak at 844 $cm^{-1}$ can be assigned to the stretching vibration of the *s*-triazine unit, indicating the chemical stability of the tri-*s*-triazine ring in g-$C_3N_4$. FTIR spectra of Cu-MOF and Zn-MOF are shown in Fig. S1b in the SI. A broad absorption can be seen in the region of 3400–3200 $cm^{-1}$, where the O–H and N–H stretching occurs. The band at 2976 $cm^{-1}$ is attributed to the stretching in the O–H group in both Cu-MOF and Zn-MOF. The stretching at 1549 $cm^{-1}$ is attributed to the C=C group, and the band at 1375 $cm^{-1}$ corresponds to the symmetric stretching of the bound –COOH group. The vibration of C–O occurs at 1052 $cm^{-1}$, the benzene ring C–H appears at 761 and 764 $cm^{-1}$, and the C=C bending vibrations are at 677 and 672 $cm^{-1}$. The reference bands for the electronic shifts observed in the final composite can be deduced from the M–O stretching frequencies at 598 and 595 $cm^{-1}$ for Cu-MOF and Zn-MOF, respectively.

The structural morphology of Cu–Zn-MOF/g-$C_3N_4$ was examined using high-resolution scanning electron microscopy (HR-SEM) and high-resolution transmission electron microscopy (HR-TEM). As shown in Fig. 2(a and b), g-$C_3N_4$ reveals a rough surface composed of numerous stacked, wrinkled, sheet-like structures that are often aggregated into larger, irregular blocks. These sheets appear thin and partially transparent at the edges, suggesting a nanosheet-like architecture with a high degree of folding. Fig. 2(c and d) illustrate that the outer morphology consists of large, irregular porous sheets decorated with small spheres accumulated with clusters of nanorods, which confirms the presence of Cu–Zn-MOF/g-$C_3N_4$. The formation of these spherical clusters occurs through a self-assembly process in which Cu and Zn ions undergo competitive coordination with organic linkers, resulting in a hierarchical architecture instead of individual metal phases. The composite confirms that the presence of Cu–Zn-MOF is intercalated on the surface of g-$C_3N_4$ sheets, where g-$C_3N_4$ provides nucleation sites that stabilize the bimetallic nodes and prevent the uncontrolled growth of large crystals. The HR-SEM image of Cu-MOF is represented in Fig. S2(a and b), which shows the rectangular microcrystals with smooth surfaces and sharp faceted edges, indicating high crystallinity. Fig. S2(d and e) shows the well-defined cubic microcrystals of Zn-MOF.

The HR-TEM study further evaluated the internal morphology of Cu–Zn-MOF/g-$C_3N_4$, as shown in Fig. 2e, which shows the typical layered and wrinkled structure of g-$C_3N_4$, providing a large surface area for metal attachment. It further reveals that the dense, high-contrast Cu–Zn-MOF nanostructures consist of interconnected nanorods, which are intimately associated with these semi-transparent sheets. The absence of discernible metal particle aggregation suggests that the Cu–Zn species are well dispersed. This template serves as a crucial source of nucleation sites, thereby stabilizing the bimetallic constituents and inhibiting unregulated growth. Fig. 2f exhibits well-distributed bimetallic areas with visible lattice fringes, confirming the crystalline structure of the Cu–Zn species and the strong contact between the MOF and the carbon nitride support. This structural integration is attributed to a self-assembly process. The g-$C_3N_4$ structure illustrates how metal centres and organic linkers interact to form a highly porous framework. This structure has accessible active sites, which improve the performance of colorimetric sensing. Fig. 2g and h show the lattice fringes of Cu–Zn-MOF/g-$C_3N_4$ with interplanar spacings of 0.134 nm and 0.201 nm. As shown by the SAED pattern (Fig. 2i), the observed diffraction spots paired in a periodic lattice illustrate that the Cu–Zn-MOF material exhibits semi-crystalline nature. These sharp reflections further imply that the long-range order within the MOF extends into the combined material with the g-$C_3N_4$ nanosheets. Furthermore, the EDX spectrum confirmed that the elements Cu, Zn, C, N and O are present in Cu–Zn-MOF/g-$C_3N_4$, as shown in Fig. S2(c, f and i) and S3.

XPS analysis was employed to examine the surface elemental chemical states of Cu–Zn-MOF/g-$C_3N_4$. As shown in Fig. 3a, the survey spectrum of the composite material exhibits the presence of elements. Cu 2p XPS region was deconvoluted to reveal the chemical states of copper. The $Cu^+$ state is evidenced by the characteristic peaks at 932.2 eV ($2p_{3/2}$) and 951.8 eV ($2p_{1/2}$). Additionally, the presence of $Cu^{2+}$ is identified by the peaks at 933.4 eV ($2p_{3/2}$) and 953.1 eV ($2p_{1/2}$). A distinct shake-up satellite centered at 941.8 eV confirms the presence of $Cu^{2+}$ species, as shown in Fig. 3b. The Zn 2p spectrum displays a characteristic doublet with binding energies at 1021.8 eV and 1044.8 eV, corresponding to the Zn $2p_{3/2}$ and Zn $2p_{1/2}$ core levels, respectively, and the spin–orbital splitting is $\Delta E$ = 23 eV, as displayed in Fig. 3c. The high-resolution C 1s spectrum, as

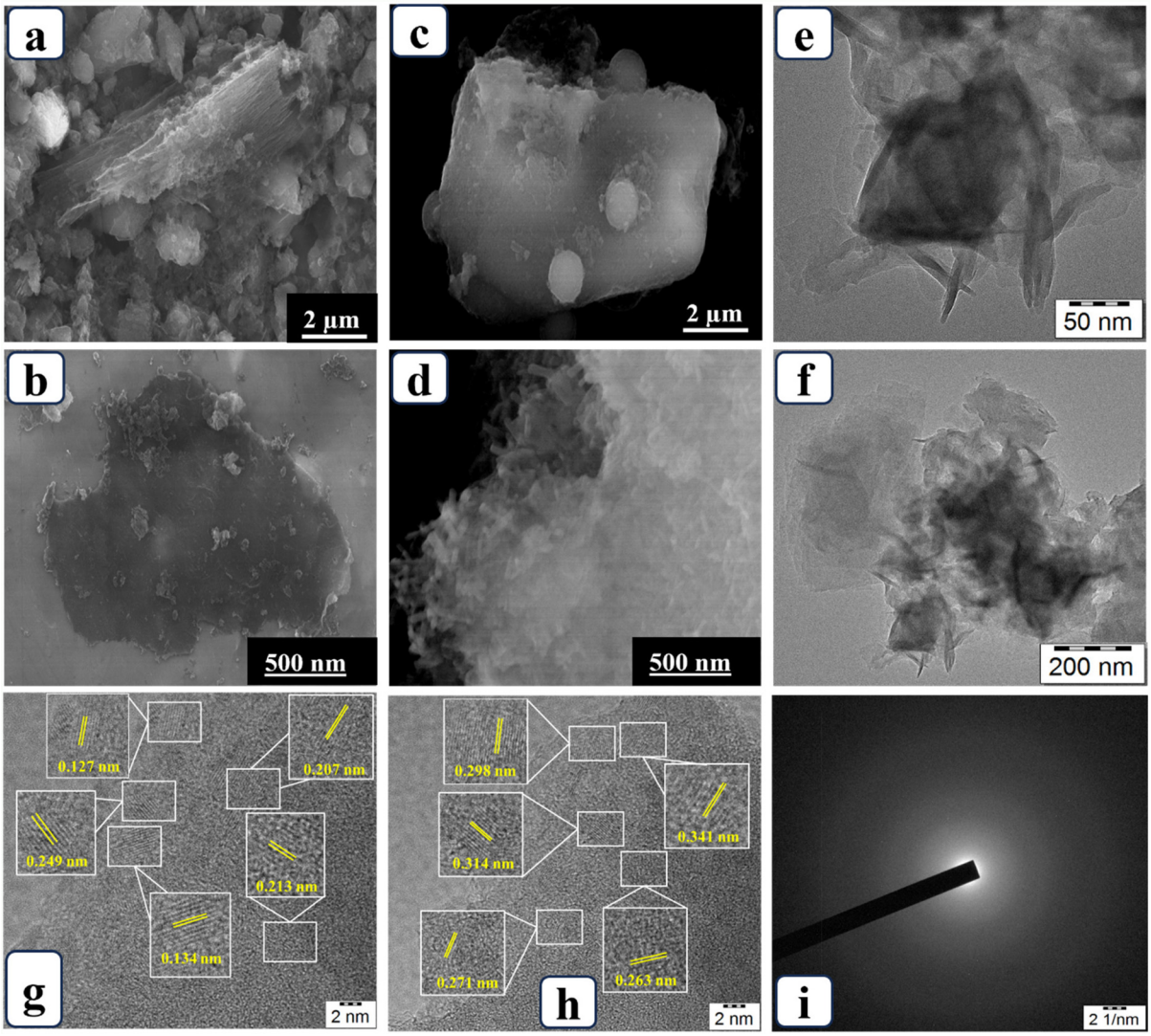


**Fig. 2** (a and b) HR-SEM images of g-$C_3N_4$ and (c and d) Cu–Zn-MOF/g-$C_3N_4$. (e and f) HR-TEM images of Cu–Zn-MOF/g-$C_3N_4$, (g) and (h) lattice fringe analysis, and (i) SAED pattern of the Cu–Zn-MOF/g-$C_3N_4$ hybrid.

depicted in Fig. 3d, was deconvoluted into three distinct components at 284.4 eV, 285.3 eV, and 288.1 eV. These three peaks are assigned to the C–C coordination of adventitious carbon, N–C–N species and $sp^2$-hybridized C within the triazine rings (N=C=N), respectively.[46] As illustrated in Fig. 3e, the N 1s spectrum was deconvoluted into three distinct components at 397.8 eV, 398.6 eV, and 399.8, assigned to the $sp^2$-hybridized nitrogen in the triazine rings (C=N–C), tertiary bridging nitrogen atoms (N-$(C)_3$), and terminal amino groups (C-$NH_x$), respectively. The dominance of the peak at 397.8 eV confirms the high degree of polymerization within the graphitic framework. The O 1s spectrum, in Fig. 3f, shows that the peak at 530.9 eV is attributed to the lattice oxygen (M–O) within the metal–organic framework. In comparison, the peak at 531.9 eV corresponds to the oxygen in the carboxyl groups (C=O). Finally, the peak at 533.1 eV is assigned to surface hydroxyl groups.[55,56]

The nitrogen adsorption–desorption study of the Cu–Zn-MOF/g-$C_3N_4$ composite exhibits a distinctive Type IV isotherm with an H3-type hysteresis loop, indicating a mesoporous structure formed by plate-like aggregates. The composite usually has an area of 90.2 $m^2$ $g^{-1}$, as shown in Fig. 4a. Barrett–Joyner–Halenda (BJH) pore size distribution verifies a highly uniform and narrow porosity with a predicted pore diameter of 1.1 nm, as shown in Fig. 4b. The observed structural arrangement implies that, despite the material's mesoporous nature, a substantial portion of its internal volume is occupied by diminutive pores situated at the mesopore boundary. This homogeneous porosity facilitates a high density of active sites, thereby substantially enhancing the material's selective adsorption capabilities and colorimetric response for antibiotic detection.

Zeta potential measurements were employed to investigate the surface charge evolution during the assembly of the com-

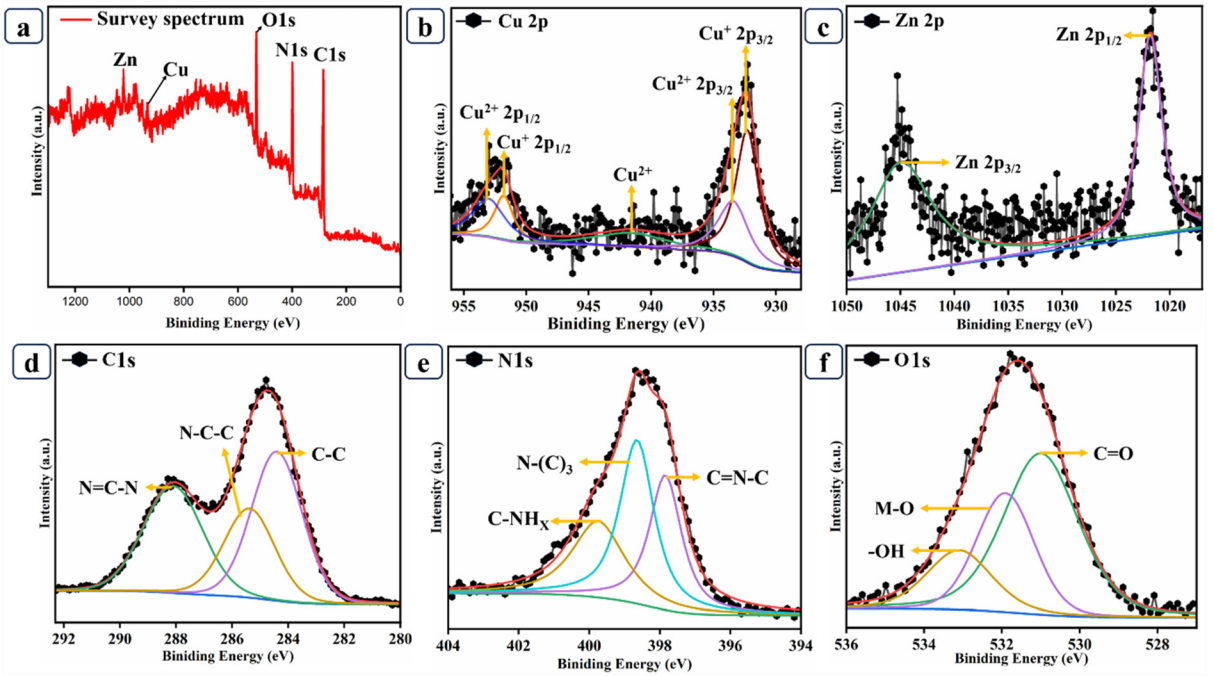


**Fig. 3** XPS spectra of Cu–Zn-MOF/g-$C_3N_4$: (a) survey, (b) Cu, (c) Zn, (d) C 1s, (e) N 1s, and (f) O 1s.

posite and the subsequent sensing mechanism, as represented in Fig. 4c. The pristine Cu–Zn-MOF exhibited a strongly negative zeta potential of −16.7 mV, whereas pure g-$C_3N_4$ displayed a positive value of +3.23 mV. Upon the formation of the composite, the zeta potential shifted to an intermediate value of −9.07 mV, confirming the successful electrostatic assembly of the negatively charged MOF with the positively charged g-$C_3N_4$ sheets. While CIP alone presented a negative potential of −13.7 mV, the introduction of the target analyte and TMB into the catalytic system resulted in a significant charge reversal to +4.73 mV. This positive shift is ascribed to the surface adsorption of cationic oxidized TMB species generated during the catalytic reaction, indicating strong electrostatic interactions within the sensing interface. The EPR spectrum of Cu–Zn-MOF/g-$C_3N_4$ shows a distinct resonance signal at a g-value of 2.07, characteristic of unpaired electrons associated with $Cu^{2+}$ centres. The paramagnetic nature of the catalyst is corroborated by the visible observation of the detected first-derivative resonance signal, which is quite consistent with the local coordination environment and further proves that these active centers are directly responsible for the peroxidase-like catalysis, as shown in Fig. 4d.[57]

### 3.2 Confirmation of ˙OH radicals and the conformation study

The peroxidase-like activity exhibited by Cu–Zn-MOF/g-$C_3N_4$ is attributed to its capacity to catalyse the breakdown of $H_2O_2$. This process produces ˙OH, which then oxidize the chromogenic substrate TMB, resulting in the formation of blue oxTMB. To confirm the generation of ˙OH, terephthalic acid was utilised as a fluorescent probe. While terephthalic acid is non-fluorescent, it reacts with ˙OH to form the highly fluorescent 2-hydroxyterephthalic acid. In Fig. 5(a and b), it can be seen that the $H_2O_2$ + Cu–Zn-MOF/g-$C_3N_4$ system exhibited strong fluorescence from 350 nm to 550 nm. The control group, in the absence of this catalyst, shows a negligible fluorescence spectrum. The results show that Cu–Zn-MOF/g-$C_3N_4$ exhibits a natural peroxidase-like activity and reacts with $H_2O_2$ through a Fenton-like pathway, giving rise to ˙OH. These reactive radicals then oxidize the chromogenic substrate TMB, producing the oxTMB for colorimetric detection. To further elucidate the reactive species involved in the catalytic process, a series of scavenger experiments were conducted. Specifically, *p*-benzoquinone (PBQ), D-histidine (D-His), and isopropyl alcohol (IPA) were employed as scavengers for superoxide radicals ($^{\bullet}O_2^-$), singlet oxygen ($^1O_2$), and hydroxyl radicals (˙OH), respectively. If any of these species contributed significantly to the catalytic reaction, the corresponding signal intensity would be expected to decrease upon the addition of the respective scavenger. As shown in Fig. 5c, the introduction of PBQ and D-His resulted in negligible changes in catalytic activity, indicating that $^{\bullet}O_2^-$ and $^1O_2$ do not play a major role in the reaction. In contrast, the presence of IPA led to a pronounced suppression of activity, confirming that ˙OH radicals are the primary reactive species responsible for the observed peroxidase-like behaviour.

### 3.3 Synergistic peroxidase-like activity in Cu–Zn-MOF/g-$C_3N_4$ relative to individual Cu and Zn-MOFs

As depicted in Fig. 5d, there is no apparent absorbance change of the TMB + $H_2O_2$ system without the Cu–Zn-MOF/g-$C_3N_4$ catalyst, and the solution is nearly colourless. After introducing Cu–Zn-MOF/g-$C_3N_4$, the solution rapidly develops an

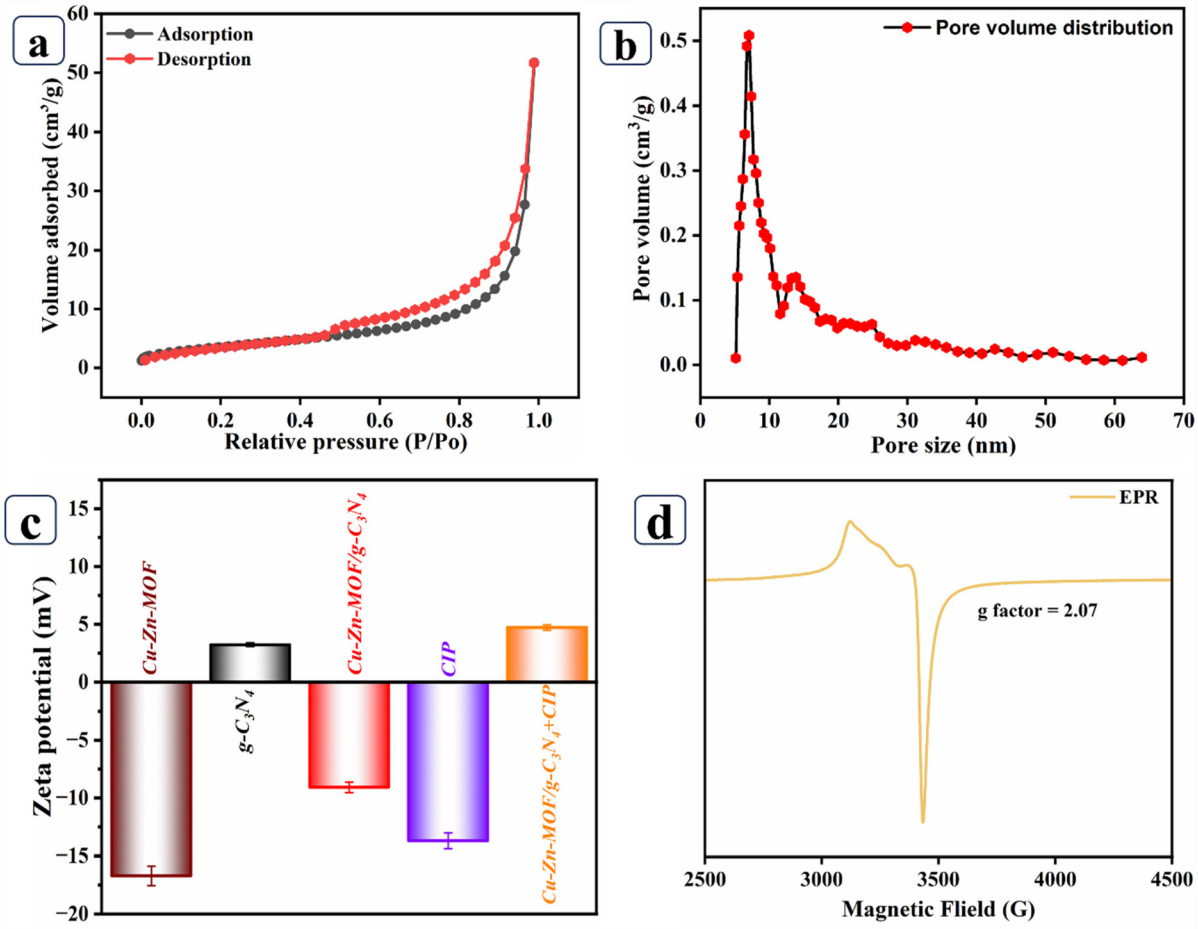


**Fig. 4** (a) $N_2$ adsorption–desorption isotherms, (b) pore size distribution of Cu–Zn-MOF/g-$C_3N_4$, (c) zeta potential of Cu–Zn-MOF, g-$C_3N_4$, Cu–Zn-MOF/g-$C_3N_4$, CIP, Cu–Zn-MOF/g-$C_3N_4$ +CIP and (d) EPR spectrum of Cu–Zn-MOF/g-$C_3N_4$.

intense blue colour, demonstrating the catalyst's ability to promote the oxidation of TMB. It is obvious that such a drastic visual change has well confirmed the peroxidase-like catalytic activity of Cu–Zn-MOF/g-$C_3N_4$. Meanwhile, a time-dependent UV-vis spectrum was utilized to reveal the catalytic process. The UV-vis spectra reveal a distinct absorption band centred at approximately 654 nm, which is characteristic of oxidized TMB. The absorbance at this wavelength increases rapidly during the initial stage of the reaction and stabilizes within 2 to 4 min showing negligible variation upon prolonged reaction time. To further elucidate the catalytic advantage of the composite material, the peroxidase-like activities of Cu-MOF, Zn-MOF and Cu–Zn-MOF were evaluated separately under identical conditions using TMB and $H_2O_2$ as substrates, as shown in Fig. 5e. Both Cu-MOF (1 mg $mL^{-1}$) and Zn-MOF (1 mg $mL^{-1}$) show a moderate increase in absorbance at 654 nm as the reaction time extends from 5 to 15 min. The peroxidase activity assay was further extended using Cu–Zn-MOF as an additional control to clarify the catalytic function of each individual component. The data indicate that despite Cu–Zn-MOF having some degree of peroxidase-like activity, it seems to still have inferior performance than Cu–Zn-MOF/g-$C_3N_4$. This clearly shows that g-$C_3N_4$ is indispensable in superior catalytic efficiency that can present better electron transfer ability during the catalytic reaction process to promote the redox cycling process by accelerating the oxidation of TMB; meanwhile, g-$C_3N_4$ featuring atomical two-dimensional morphology would have a larger surface area and improved dispersibility of active Cu–Zn-MOF sites. Therefore, the synergistic interaction between Cu–Zn-MOF and g-$C_3N_4$ greatly improves the generation of reactive oxygen species. Nevertheless, their catalytic responses are markedly weaker than those of Cu–Zn-MOF/g-$C_3N_4$, even when the composite is applied at a lower concentration (0.5 mg $mL^{-1}$). Additionally, previously published nanomaterials containing copper and zinc ions, such as Cu@Co-MOFs, MOF-808-EDTA-Cu, and Cu NCs@Zn-MOF, serve as enzyme analogues. The copper and zinc in Cu–Zn-MOF/g-$C_3N_4$ are probably very important for the reaction that breaks down TMB with $H_2O_2$.[58–60] This enhanced performance can be attributed to the synergistic coupling of Cu and Zn active sites along with electron-transfer facilitation provided by the g-$C_3N_4$ framework, which together substantially improve the overall peroxidase-like activity of the hybrid catalyst (Scheme 2).

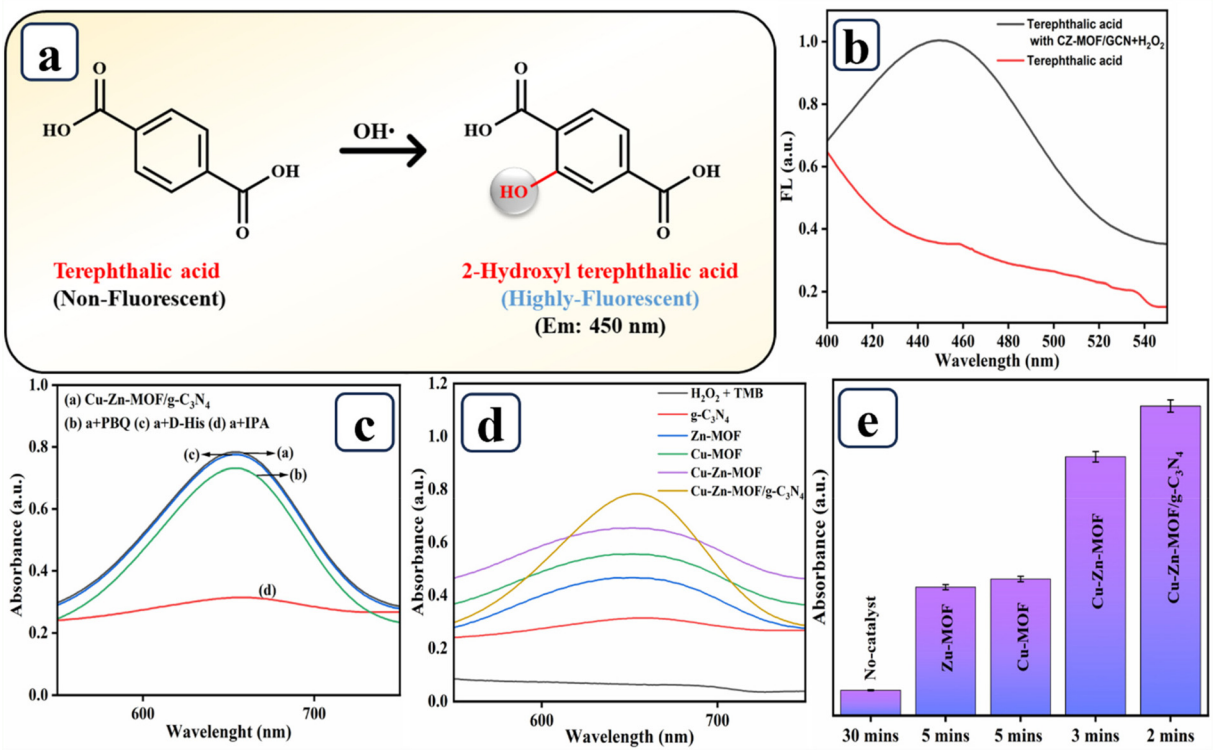


**Fig. 5** (a) Schematic representation of the hydroxylation reaction between ˙OH radicals and terephthalic acid to form the fluorescent product 2-hydroxyterephthalic acid (TAOH). (b) Fluorescence emission spectra of TAOH. (c) Peroxidase activity of Cu–Zn-MOF/g-$C_3N_4$ compared to that of the individual catalysts. (d) TMB oxidation by the individual catalysts. (e) ROS trapping experiments.

### 3.4 Role of Cu–Zn-MOF/g-$C_3N_4$

The Cu–Zn-MOF/g-$C_4N_4$ composites are capable of producing OH by adopting a Fenton-like reaction pathway to decompose $H_2O_2$. In the catalysis system presented here, the $H_2O_2$ molecules are initially adsorbed onto the large surface area of the Cu–Zn-MOFs and the support g-$C_3N_4$ nanosheets, resulting in O–O bond cleavage and reactive OH generation. These radicals then oxidize the TMB substrate, resulting in a blue charge-transfer product. In this system, the Cu centres act as the main active sites for breaking down $H_2O_2$, similar to the Fenton reaction. The Zn ions and the nitrogen-rich g-$C_3N_4$ structure help substrate adsorption and facilitate electron transfer at the interface of the two materials. The electronic interaction between the bimetallic framework nodes and the graphitic support in the Cu–Zn-MOF/g-$C_3N_4$ structure reduces the energy needed to create radicals. The synergistic effect of copper and zinc ions in the g-$C_3N_4$ network effectively potentiates the peroxidase model activity toward $H_2O_2$ and efficiently facilitates the oxidation of TMB, as shown in Fig. 6.

$$Cu^{2+} + H_2O_2 + H^+ \longrightarrow Cu^+ + \bullet OH + OH^-$$

$$\bullet OH + TMB \longrightarrow oxTMB$$

**Scheme 2** Illustration of the possible reaction mechanism of the Cu–Zn-MOF/g-$C_3N_4$ nanozyme.

### 3.5 Optimization of the colorimetric sensor

To improve the colorimetric detection of CIP, the experimental conditions for the Cu–Zn-MOF/g-$C_3N_4$ sensor were carefully studied. Fig. 7a shows the acidity of the medium where pH values from 2 to 8 were indicated. The optimal catalytic activity appears at p H 4.0. Besides, as the concentration of Cu–Zn-MOF/g-$C_3N_4$ in the solution prepared increased from 0. 1 mg $mL^{-1}$ to 0.6 mg $mL^{-1}$, the absorbance increased significantly. When it was 0.4 mg $mL^{-1}$, the signal became stable, which was the optimal loading for better peroxidase-like activity, as shown in Fig. 7b. In addition, the concentration of the TMB substrate was adjusted to optimize analytical sensitivity. The absorbance readings increased consistently, peaking at 40 μM, which was determined to be the optimal concentration for the chromogenic reaction, as illustrated in Fig. 7c. The impact of temperature was investigated. It demonstrated that the UV light absorption by the sensor was highest at 35 °C (Fig. 7d) and over 35 °C, its activity greatly decreased. Therefore, in all subsequent utilization of the sensor, the chosen conditions were pH 4.0, 0.4 mg $mL^{-1}$ of the catalyst, 40 μM TMB and 35 °C.

### 3.6 Catalytic mechanism of MOF-based peroxidase-like activity

The peroxidase-like activity of the Cu–Zn-MOF/g-$C_3N_4$ nanozyme was examined with (TMB) as a chromogenic substrate with $H_2O_2$. As shown in Scheme 2, the reaction proceeded through concurrent Fenton-like processes between the Cu and

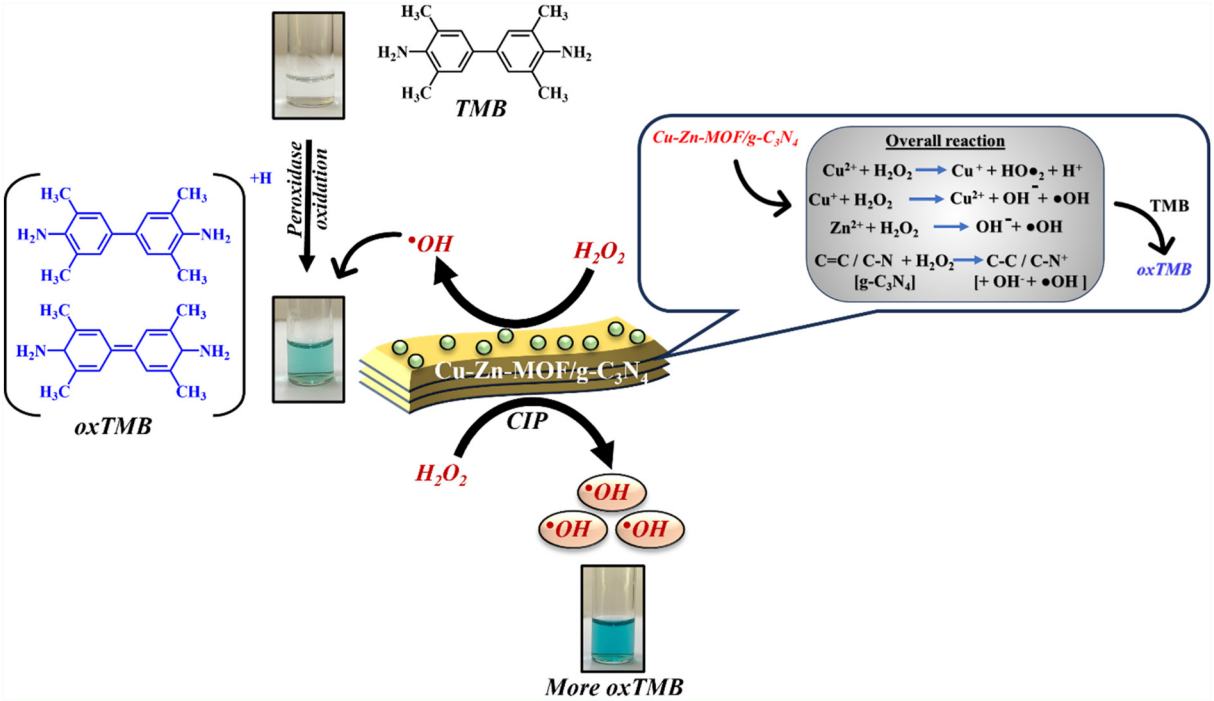


Fig. 6 Graphical representation of the proposed catalytic mechanism of Cu–Zn-MOF/g-$C_3N_4$ for TMB oxidation using $H_2O_2$.

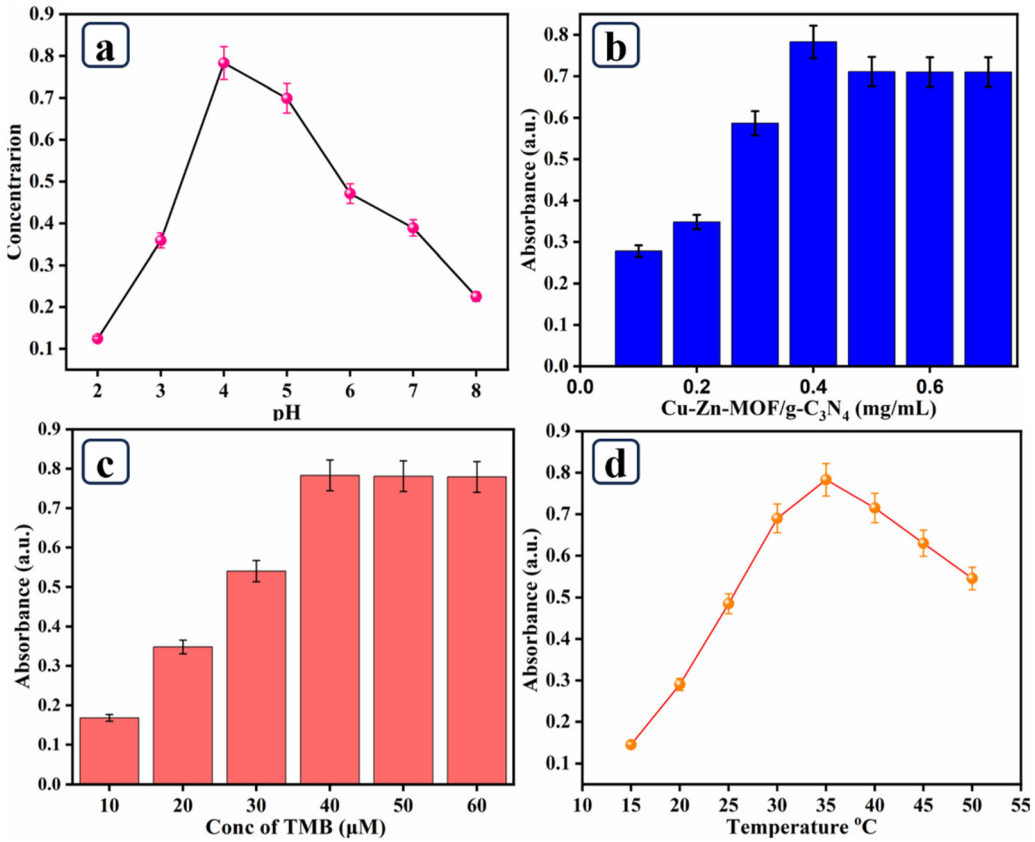


Fig. 7 Optimization of (a) pH, (b) amount of Cu–Zn-MOF/g-$C_3N_4$, (c) TMB concentration, and (d) temperature.

**Step 1: $H_2O_2$ Activation via Peroxidase-Like Activity**

$$\text{Cu-Zn-MOF/g-}C_3N_4 + H_2O_2 \longrightarrow \bullet OH + OH^-$$

**Step 2: Oxidation of TMB (Color Development)**

$$\bullet OH + \text{TMB} \longrightarrow \text{oxTMB (Blue color)}$$

**Step 3: CIP-Induced Signal Enhancement**

$$\text{TMB} + \text{CIP} \longrightarrow \text{oxTMB (Dark Blue) CIP}$$

**Scheme 3** Schematic illustration of the sensing reaction of the proposed colorimetric sensor.

the Zn metal centres of the MOF framework. Under acidic conditions, the metal sites provided by MOFs enable the homolytic cleavage of $H_2O_2$, resulting in the formation of reactive $^{\bullet}OH$, which then oxidize colorless TMB to oxTMB, showing an absorption peak at 654 nm. Interestingly, the peroxidase activities of Cu–Zn-MOF/g-$C_3N_4$ were markedly enhanced by the addition of CIP (Scheme 3). After the addition of CIP, the system displayed a color change from blue to dark blue with a remarkable increase in absorption intensity, indicating an excellent oxidation-stimulating effect. This enhancement could be ascribed to the facilitated electron transfer by the

**Table 1** Real sample analysis of CIP in water

| Sample | Spiked (nM) | Detected CIP ± SD | Recovery (%) |
|---|---|---|---|
| Unspiked drinking water | 0 | 0 | 0 |
| Drinking water | 2 | 2.013 ± 0.21 SD | 100.6 |
| | 4 | 3.94 ± 0.41 SD | 98.5 |
| Unspiked tap water | 0 | 0 | 0 |
| Tap water | 5 | 4.89 ± 0.74 SD | 99.2 |
| | 10 | 10.15 ± 0.34 SD | 101.4 |
| Unspiked lake water | 0 | 0 | 0 |
| Lake water | 50 | 48.74 ± 0.87 SD | 97.7 |
| | 100 | 100.12 ± 0.75 SD | 100.1 |

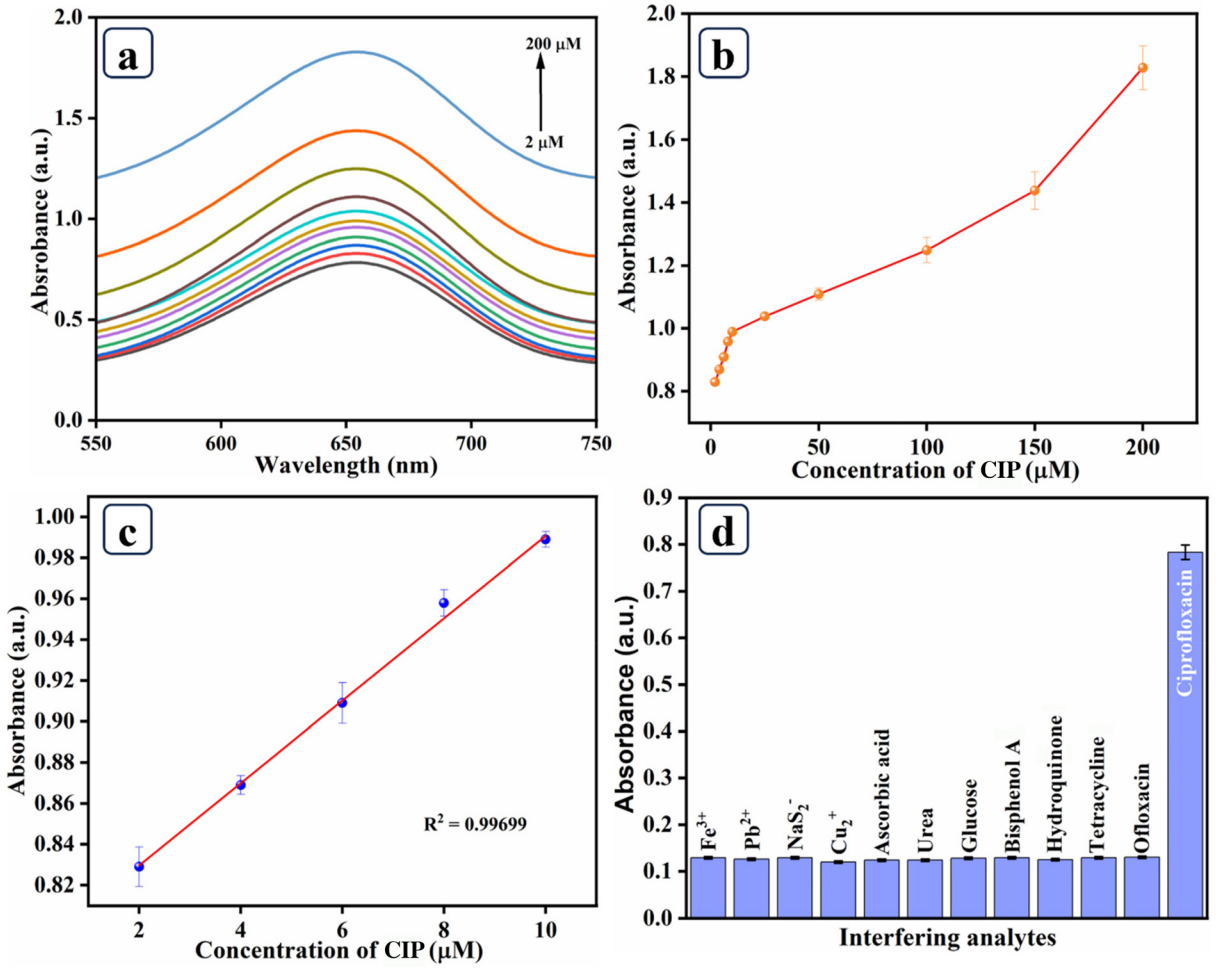


**Fig. 8** (a) Sensitivity analysis of the Cu–Zn-MOF/g-$C_3N_4$ nanozyme for the detection of CIP through a sensitivity plot. (b and c) Linear relationship plots between the concentration of CIP and the absorbance intensity. (d) Selectivity analysis of the Cu–Zn-MOF/g-$C_3N_4$ nanozyme + TMB + $H_2O_2$ colorimetric system with various interfering analytes for CIP detection.

complexation of the Cu and Zn centres with the nitrogen heterocyclic rings and piperazine groups of the CIP molecule. Meanwhile, the carbonyl and carboxylate groups of the CIP molecule could supply an anionic chelation site and further stabilize the CIP molecule on the catalytic surface. The multidentate interaction between the complex and the CIP molecule benefited from the surface adherence, leading to efficient ROS generation and the amplification of the colorimetric response for highly sensitive detection of CIP.

### 3.7 Sensitivity and selectivity analysis

The sensitivity and selectivity of the Cu–Zn-MOF/g-$C_3N_4$ composite toward CIP were rigorously evaluated using a colorimetric sensing strategy, which facilitated rapid visual detection

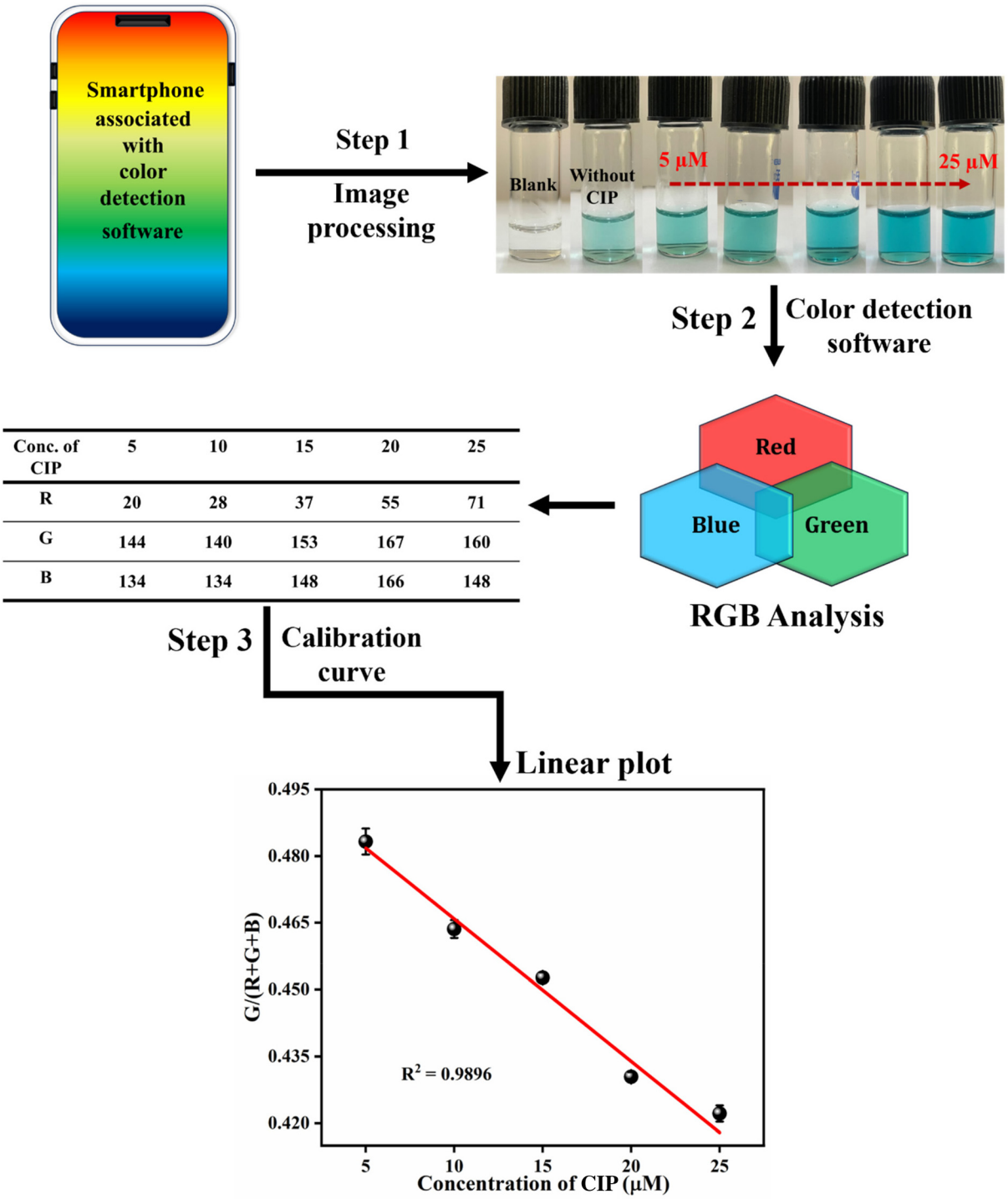


| Conc. of CIP | 5 | 10 | 15 | 20 | 25 |
|---|---|---|---|---|---|
| R | 20 | 28 | 37 | 55 | 71 |
| G | 144 | 140 | 153 | 167 | 160 |
| B | 134 | 134 | 148 | 166 | 148 |

Fig. 9 Smartphone-integrated colorimetric platform for CIP detection using Cu–Zn-MOF/g-$C_3N_4$ nanozymes.

through a distinct, concentration-dependent color transition. UV-vis spectroscopic analysis corroborated this visual change, revealing a significant enhancement in absorbance intensity as the CIP concentration increased from 2 to 200 μM within the Cu–Zn-MOF/g-$C_3N_4$ + TMB + $H_2O_2$ system, as shown in Fig. 8a. A robust linear correlation between the absorbance response and the CIP concentration was observed across this broad analytical range, signifying highly dependable quantitative detection, as illustrated in Fig. 8b. Specifically, a remarkable linear correlation coefficient was achieved within the 2–10 μM range, as shown in Fig. 8c, and the LOD, determined *via* the 3 per slope method, proved highly competitive compared to various nanomaterial-based colorimetric and electrochemical sensors listed in Table S1. To assess the specificity of the platform, selectivity studies were conducted against a suite of potential interferents, including structural antibiotic analogs, metal ions, and common organic compounds, as shown in Fig. 8d. Compared to the robust signal triggered by CIP, these interfering species produced negligible changes in color intensity and absorbance, confirming the excellent selectivity of the sensing platform. This high specificity is likely attributed to the molecular structure of CIP, which promotes preferential binding and subsequent signal amplification. Collectively, these results demonstrate that the Cu–Zn-MOF/g-$C_3N_4$ composite functions as an efficient and reliable colorimetric sensor. $Fe^{3+}$ and $Cu^{2+}$ interferences were successfully eliminated by employing their strong masking agents NaF and $Na_2S_2O_3$, respectively. NaF and $Na_2S_2O_3$ played a role in effectively masking the interference caused by $Fe^{3+}$ and $Cu^{2+}$. Its rapid response time and high analytical performance highlight its significant potential for real-world applications in environmental monitoring, pharmaceutical quality control, and wastewater analysis, offering a versatile tool for the sensitive detection of antibiotic residues.

### 3.8 Determination of CIP in water samples

To examine the feasibility of the $H_2O_2$ + TMB + Cu–Zn-MOF/g-$C_3N_4$ to determine the CIP in real samples, drinking, tap and lake water were collected from SRMIST. The contaminants were removed by filtering the samples through a 0.2 μm membrane. The samples were spiked with various concentrations of CIP ranging from 0 to 20 μM. Table 1 illustrates that the three distinct concentrations of CIP in spiked actual samples were measured, with recoveries ranging from 97.7 to 102%. These results confirmed that $H_2O_2$ + TMB + Cu–Zn-MOF/g-$C_3N_4$ is accurate and dependable for CIP detection in water samples.

### 3.9 Cu–Zn-MOF/g-$C_3N_4$ nanozyme-based smartphone sensor for the detection of CIP *via* RGB analysis

To enhance the colorimetric probe as an advanced analytical tool, the study included an RGB analysis using a smartphone (Fig. 9). Digital images of the blue solutions were captured after the colorimetric reaction. These images were processed using color detector software to quantify the Red (R), Green (G), and Blue (B) components for each sample spanning a spectrum of analyte concentrations. In order to account for the effect of environmental lighting, a linear calibration curve was plotted by comparing the normalized G/(R + G + B) green channel ratio with the concentration of the analyte of interest. These analyses demonstrated a robust linear relationship across the concentration spectrum from 5 to 25 μM, and the limit of detection (LOD) was 4.4 μM. Thus, the results confirm that the proposed probe, using a smartphone as the detection platform, is a suitable, easily accessible, and portable method for the rapid detection of the analyte in real samples.

### 3.10 Recyclability and stability analysis

The stability and reusability of the prepared nanozyme Cu–Zn-MOF/g-$C_3N_4$ were also investigated. The Cu–Zn-MOF/g-$C_3N_4$ nanozyme was derived from the colorimetric measurement by a regular centrifugation method and then dried at 60 °C for the reusability test. After undergoing the same step as the peroxidase activity, the product reached a relative activity of approximately 99.4% compared to the first-run sample. Likewise, after 4 sequential runs, the activity dropped to 87.8%, as illustrated in Fig. S4(a). The peroxidase properties of the sensor were recorded in the course of a 15-day stability study, which exhibited a reduction in overall catalyst activity of only 32%, as shown in Fig. S4(b).

## 4. Conclusions

In summary, a novel bimetallic Cu–Zn-MOF/g-$C_3N_4$ hybrid nanozyme was synthesized by a simple solvothermal method showing excellent peroxidase-like activity for highly sensitive CIP detection. Structural characterization showed that Cu–Zn-MOF particles were uniformly dispersed on the surface of g-$C_3N_4$ nanosheets as the substrate. The outstanding catalytic activity was derived from the synergistic Fenton-like catalytic pathway, which oxidized TMB by $^{\bullet}OH$ formed at the bimetallic active sites of the Cu–Zn-MOF. The sensing system worked through CIP-inhibited TMB oxidation with an LOD of 0.66 μM. Beyond simple colorimetric sensing, this work also successfully introduced a handheld, smartphone-enabled analytical platform. The visible color change was captured, and RGB data were processed using a digital conversion model, which provided a practical LOD of 4.4 μM. The combination of a high-performance nanozyme material and mobile-phone colorimetry offers an inexpensive and accessible methodology that bypasses the need for sophisticated laboratory instrumentation. By replacing costly, unstable natural enzymes with a stable MOF-based composite, this study lays the foundation for a flexible, rapid, on-site monitoring approach for the direct quantification of antibiotic contamination in environmental and clinical applications.

## Author contributions

Surendhar Sasikumar: methodology, resources, software, visualization, writing – original draft, and formal analysis.

Arunjegan Amalraj: investigation, visualization, and formal analysis. Panneerselvam Perumal: guidance, investigation, visualization, and supervision.

## Conflicts of interest

The authors have no relevant financial or non-financial interests to disclose.

## Data availability

Data provided in the manuscript and the supplementary information (SI) are also available on request from the corresponding author.

Supplementary information (SI) is available. Supplementary information includes the Instrumentation, XRD, FTIR, SEM, Elemental mapping, Recyclability, and Comparision table. See DOI: https://doi.org/10.1039/d6an00320f.

## Acknowledgements

The authors acknowledge the financial support from the Department of Chemistry and the instrumentation facilities provided by SCIF, NRC, and PNCF, SRM Institute of Science and Technology, Kattankulathur-603 203, Tamil Nadu, India.

## References

1 M. Cycoń, A. Mrozik and Z. Piotrowska-Seget, *Front. Microbiol.*, 2019, **10**, 412419.
2 P. Barathe, K. Kaur, S. Reddy, V. Shriram and V. Kumar, *J. Hazard. Mater. Lett.*, 2024, **5**, 100105.
3 D. G. J. Larsson and C. F. Flach, *Nat. Rev. Microbiol.*, 2021, **20**, 257.
4 Q. Yang, Y. Gao, J. Ke, P. L. Show, Y. Ge, Y. Liu, R. Guo and J. Chen, *Bioengineered*, 2021, **12**, 7376–7416.
5 S. I. Polianciuc, A. E. Gurzău, B. Kiss, M. Georgia Ștefan and F. Loghin, *Med. Pharm. Rep.*, 2020, **93**, 231–240.
6 C. Ching and M. H. Zaman, *Sci. Rep.*, 2020, **10**(1), 8754.
7 T. Huang, Y. Xu, J. Zeng, D. H. Zhao, L. Li, X. P. Liao, Y. H. Liu and J. Sun, *Front. Microbiol.*, 2016, **7**, 212753.
8 T. Liu, W. Liu, X. Li, H. Wang, Y. Lan, S. Zhang, Y. Wang and H. Liu, *Sci. Rep.*, 2024, **14**(1), 19831.
9 A. Hayes, L. May Murray, I. Catherine Stanton, L. Zhang, J. Snape, W. Hugo Gaze and A. Kaye Murray, *Environ. Int.*, 2022, **169**, 107488.
10 R. Laxminarayan and R. R. Chaudhury, *PLoS Med.*, 2016, **13**, e1001974.
11 D. Viola, M. Ayan, D. Prachi, M. Matthias, B. Ivan, U. Christian, N. Kayzad, R. Camilla, W. C. Derrick, C. CRyPTIC, R. Jean-Philippe, W. Thierry, M. Nerges and N. Stefan, *Genome Med.*, 2022, **14**, 95.
12 L. Zhang, S. Tang, F. He, Y. Liu, W. Mao and Y. Guan, *Chem. Eng. J.*, 2019, **378**, 122215.
13 P. Zheng, M. Li, R. Jurevic, S. K. Cushing, Y. Liu and N. Wu, *Nanoscale*, 2015, **7**, 11005–11012.
14 Z. Vybíralová, M. Nobilis, J. Zoulova, J. Květina and P. Petr, *J. Pharm. Biomed. Anal.*, 2005, **37**, 851–858.
15 B. Liu, Y. Huang, Q. Shen, X. Zhu, Y. Hao, P. Qu and M. Xu, *RSC Adv.*, 2016, **6**, 100743–100747.
16 Q. Wang, F. Yang, L. Xiong, C. Li, Z. He, J. Wang, K. Sun and G. Deng, *Mikrochim. Acta*, 2025, **192**, 799.
17 M. K. Matta, A. Chockalingam, A. Gandhi, S. Stewart, L. Xu, K. Shea, V. Patel and R. Rouse, *Anal. Methods*, 2018, **10**, 1237–1246.
18 M. Azriouil, M. Matrouf, F. E. Ettadili, F. Laghrib, A. Farahi, S. Saqrane, M. Bakasse, S. Lahrich and M. A. El Mhammedi, *Food Chem. Toxicol.*, 2022, **168**, 113378.
19 S. Sadeghi and J. Javanshiri-Ghasemabadi, *RSC Adv.*, 2024, **14**, 7836–7849.
20 S. Naveed and N. Waheed, *Mintage Journal of Pharmaceutical & Medical Sciences*, 2014, **3**, 10.
21 K. Murugan, P. Suresh, A. Amalraj, G. raj Muniyandi, N. Pugazhenthiran and A. Thirugnanasambandam, *Langmuir*, 2025, **41**, 17924–17937.
22 N. G. Balasubramaniyan, N. P. Singh Chauhan and P. Perumal, *J. Electroanal. Chem.*, 2025, **978**, 118899.
23 V. Shukla, M. Ahmad and K. A. Siddiqui, *Mater. Today Chem.*, 2024, **38**, 102138.
24 M. Alizadeh Sani, G. Jahed-Khaniki, N. Shariatifar, A. Khezerlou, A. Abedini, M. Rezvani-Ghalhari, S. Hassani, M. Tavassoli and D. J. McClements, *ACS Food Sci. Technol.*, 2024, **4**, 2272–2300.
25 Z. Wang, Y. Huang, K. Xu, Y. Zhong, C. He, L. Jiang, J. Sun, Z. Rao, J. Zhu, J. Huang, F. Xiao, H. Liu and B. Y. Xia, *Nat. Commun.*, 2023, **14**(1), 69.
26 B. Yu, Y. Bai, W. Gao, J. Wei, C. Gao, X. Ma and P. Zhu, *Food Chem.*, 2025, **486**, 144592.
27 H. Lan, J. Niu, T. Luo, L. Wang and X. Hou, *Langmuir*, 2025, **41**, 8060–8070.
28 H. Li, Y. Zhang, J. Zhang, K. Huo, J. Gu, Y. Zhou, Y. Liu, Y. Liu and X. Liu, *Microchem. J.*, 2024, **199**, 110098.
29 A. Mechoor, S. Berchmans and G. Venkatachalam, *ACS Omega*, 2023, **8**, 39636–39650.
30 Y. Lou, J. Chen, L. Sun, S. Chen, Z. Yang, M. Li, R. Cao and J. Tian, *Anal. Chem.*, 2025, **97**, 17204–17215.
31 K. S. Novoselov, A. K. Geim, S. V. Morozov, D. Jiang, Y. Zhang, S. V. Dubonos, I. V. Grigorieva and A. A. Firsov, *Science*, 2004, **306**, 666–669.
32 M. Ullah, S. Ganesan, B. Kumari, M. Zafar, K. Yusuf, S. A. Hussein, S. K. Issa, F. H. Alsultany, M. Singh, L. Zhengxin and S. Ullah, *Ionics*, 2024, **30**, 6705–6718.
33 M. Lu, Z. Wang, W. Xie, Z. Zhang, L. Su, Z. Chen and Y. Xiong, *Anal. Bioanal. Chem.*, 2023, **415**(24), 5949–5960.
34 Y. Yu and H. Huang, *Chem. Eng. J.*, 2023, **453**, 139755.
35 N. Kumar Ravikumar, N. P. Singh Chauhan and P. Perumal, *Dalton Trans.*, 2025, **54**, 18046–18063.

 

36 Z. Chi, S. Chu, B. Wang, Z. Zhang, G. Liu and X. Wang, *Talanta*, 2026, **297**, 128591.
37 K. Murugan and A Natarajan, *Anal. Methods*, 2024, **16**, 3413–3429.
38 M. Raghunathan, A. Kapoor, P. Kumar, A. Laxshmivarahan, S. C. Tripathi, I. Ahmad and D. B. Pal, *Luminescence*, 2024, **39**, e4833.
39 N. Xu, S. Jin and L. Wang, *Rev. Anal. Chem.*, 2020, **40**, 1–11.
40 J. G. Lee, J. Hong, Y. Lee, W. J. Lee, T. Y. Jeong and J. W. Oh, *ACS Sens.*, 2025, **10**, 986–994.
41 M. Shahbaz, B. Dar, S. Sharif, M. Aqib Khurshid, S. Hussain, B. Riaz, M. Musaffa, H. Khalid, A. Rashid Ch and A. Mahboob, *RSC Adv.*, 2024, **14**, 9819–9847.
42 L. Yu and N. Li, *Chemosensors*, 2019, **7**, 53.
43 Z. Zhang, Z. Li, Z. Li, Y. Liu, R. Liu and J. Han, *Microchem. J.*, 2025, **218**, 115708.
44 P. Sharma, M. Ahmad, N. Haq, D. Dewangan, R. Medishetty, A. K. Astakala, N. Lee and K. A. Siddiqui, *ACS Appl. Bio Mater.*, 2025, **8**, 8230–8249.
45 K. Murugan and A. Natarajan, *Anal. Methods*, 2024, **16**, 3413–3429.
46 E. A. Alabdullkarem and J. Khan, *RSC Adv.*, 2025, **15**, 23801–23818.
47 B. Danagody, N. Bose, K. Rajappan, A. Iqbal, G. M. Ramanujam and A. K. Anilkumar, *ACS Biomater. Sci. Eng.*, 2023, **10**, 468–481.
48 H. Esfandian, M. Pakzad and F. Afaridoun, *J. Energy Storage*, 2024, **96**, 112692.
49 P. Patel, B. Parmar, R. I. Kureshy, N. U. H. Khan and E. Suresh, *Dalton Trans.*, 2018, **47**, 8041–8051.
50 B. Parmar, Y. Rachuri, K. K. Bisht and E. Suresh, *Inorg. Chem.*, 2017, **56**, 10939–10949.
51 R. A. Rather and Z. N. Siddiqui, *RSC Adv.*, 2019, **9**, 15749–15762.
52 K. I. Hadjiivanov, D. A. Panayotov, M. Y. Mihaylov, E. Z. Ivanova, K. K. Chakarova, S. M. Andonova and N. L. Drenchev, *Chem. Rev.*, 2020, **121**, 1286–1424.
53 K. Nakamoto, *Infrared and Raman Spectra of Inorganic and Coordination Compounds: Part A: Theory and Applications in Inorganic Chemistry: Sixth Edition*, 2008, pp. 1–419.
54 X. Lu, Z. Yue, H. Chen, S. Liu, S. Wei and Z. Wang, *Dalton Trans.*, 2025, **54**, 4956–4964.
55 P. Rohilla, B. Pal and R. K. Das, *Heliyon*, 2023, **9**, e21900.
56 N. Iqbal, A. Afzal, I. Khan, M. S. Khan and A. Qurashi, *Sci. Rep.*, 2021, **11**(1), 16886.
57 C. C. Ding, Y. Q. Li, Y. J. Sun, W. Jin, T. Liu and J. S. Hu, *Inorg. Chem.*, 2025, **64**, 14063–14072.
58 Y. Yu, X. M. Zhang, J. P. Ma, Q. K. Liu, P. Wang and Y. Bin Dong, *Chem. Commun.*, 2014, **50**, 1444–1446.
59 Y. Gu, J. Han, N. Zhang, W. Yan, Y. Guo, H. Tan, C. Yang, F. Wang and H. Yao, *ACS Appl. Nano Mater.*, 2024, **7**, 24683–24696.
60 H. Li, Y. Wu, Z. Xu and Y. Wang, *ACS Sens.*, 2024, **9**, 4701–4710.